Journal of Colloid and Interface Science 634 (2023) 195–208

Contents lists available at ScienceDirect

Journal of Colloid and Interface Science

journal homepage: www.elsevier.com/locate/jcis

An efficient and multifunctional S-scheme heterojunction photocatalyst constructed by tungsten oxide and graphitic carbon nitride: Design and mechanism study

Yaru Shang [a], Chunliang Wang [b], Chunshuang Yan [a,*], Fengyang Jing [a], Morteza Roostaeinia [c], Yu Wang [a,*], Gang Chen [a], Chade Lv [a]

[a] MIIT Key Laboratory of Critical Materials Technology for New Energy Conversion and Storage, School of Chemistry and Chemical Engineering, Harbin Institute of Technology, Harbin 150001, PR China
[b] State Key Laboratory of Applied Optics, Changchun Institute of Optics, Fine Mechanics and Physics, Chinese Academy of Sciences, Changchun 130033, PR China
[c] Department of Chemical and Petroleum Engineering, University of Calgary, 2500 University Drive, NW, Calgary, Alberta T2N 1N4, Canada

HIGHLIGHTS

- S-scheme $W_{18}O_{49}$/g-C_3N_4 heterojunction multifunctional photocatalyst was developed.
- S-scheme heterojunction improved carriers separation and redox ability of catalyst.
- FDTD revealed the expanded light absorption intensity and range for $W_{18}O_{49}$/g-C_3N_4.
- The H_2 yield rate of W20-CNNT (4.67 mmol·g^{-1}·h^{-1}) is 15.1 times that of Bulk-CN.
- W20-CNNT exhibited rapid photocatalytic degradation and bactericidal properties.

GRAPHICAL ABSTRACT

The S-scheme $W_{18}O_{49}$/g-C_3N_4 heterojunction multifunctional photocatalyst was synthesized, showing efficient and rapid photocatalytic hydrogen production, degradation (RhB) and bactericidal (*E. coli*) properties. The reasons for the improved photocatalytic performances were systematically analyzed.

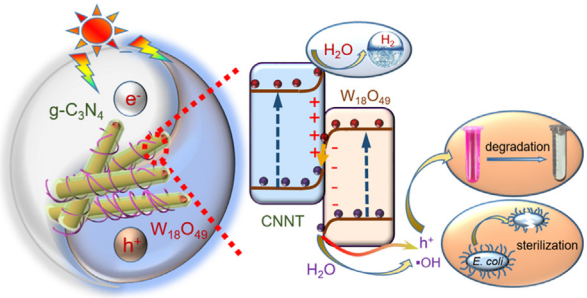

ARTICLE INFO

Article history:
Received 29 September 2022
Revised 19 November 2022
Accepted 8 December 2022
Available online 12 December 2022

Keywords:
g-C_3N_4
$W_{18}O_{49}$
S-scheme heterojunction
Photocatalysis
Multifunctional photocatalyst

ABSTRACT

The design of multifunctional photocatalyst with strong redox performance is the key to achieve sustainable utilization of solar energy. In this study, an elegant S-scheme heterojunction photocatalyst was constructed between metal-free graphitic carbon nitride (g-C_3N_4) and noble-metal-free tungsten oxide ($W_{18}O_{49}$). As-established S-scheme heterojunction photocatalyst enabled multifunctional photocatalysis behavior, including hydrogen production, degradation (Rhodamine B) and bactericidal (Escherichia coli) properties, which represented extraordinary sustainability. Finite-difference time-domain (FDTD) simulations manifested that the integration of double-layer hollow g-C_3N_4 nanotubes with $W_{18}O_{49}$ nanowires could expand the light harvesting ability. Demonstrated by density functional theory (DFT) calculations and electron spin resonance (ESR) measurements, the S-scheme heterojunction not only promoted the separation of carriers, but also improved the redox ability of the catalyst. This work provides a theoretical basis for enhancing the photocatalytic performances and broadening the application field of photocatalysis.

* Corresponding authors.
E-mail addresses: csyan@hit.edu.cn (C. Yan), wangyu1012@hit.edu.cn (Y. Wang).

https://doi.org/10.1016/j.jcis.2022.12.039
0021-9797/

1. Introduction

The utilization of solar energy through photocatalytic technology, including photocatalytic oxidation and photocatalytic reduction reactions, has been considered an ideal way to solve the problems of energy shortage and environmental pollution [1–3]. Among various photocatalytic reduction reactions, photocatalytic hydrogen (H_2) evolution by splitting water is currently-one of the most promising technologies to produce clean energy [4]. As for the photocatalytic oxidation process, the as-generated active free radicals can not only degrade organic pollutants in wastewater, but also effectively kill bacteria in wastewater without any side effects [5]. The exploration of high-efficiency and low-cost photocatalysts is achievable for sustainable development in the field of photocatalysis. In particular, the synergistic effect of photocatalytic redox is widely utilized to design high-efficiency and multifunctional catalysts for photocatalytic hydrogen production, pollutants degradation and sterilization [6,7]. Metal-free graphite carbon nitride (g-C_3N_4) is non-toxic, low cost, highly stable in acidic/basic environment, and responsive to visible light [8–10], making it a potential photocatalyst material. However, the poor light utilization, low density of active sites, sluggish electron-hole separation kinetics are still the main challenges for pristine g-C_3N_4 material to meet this "one stone, three birds" multifunctional photocatalysis.

It is worth noting that the design and construction of heterojunction photocatalysts with appropriate band alignment can enhance separation efficiency of electrons and holes and improve the utilization of light. In addition, the synergistic effect of photocatalytic redox based on the conduction band (CB) and valence band (VB) positions of the materials can further promote the

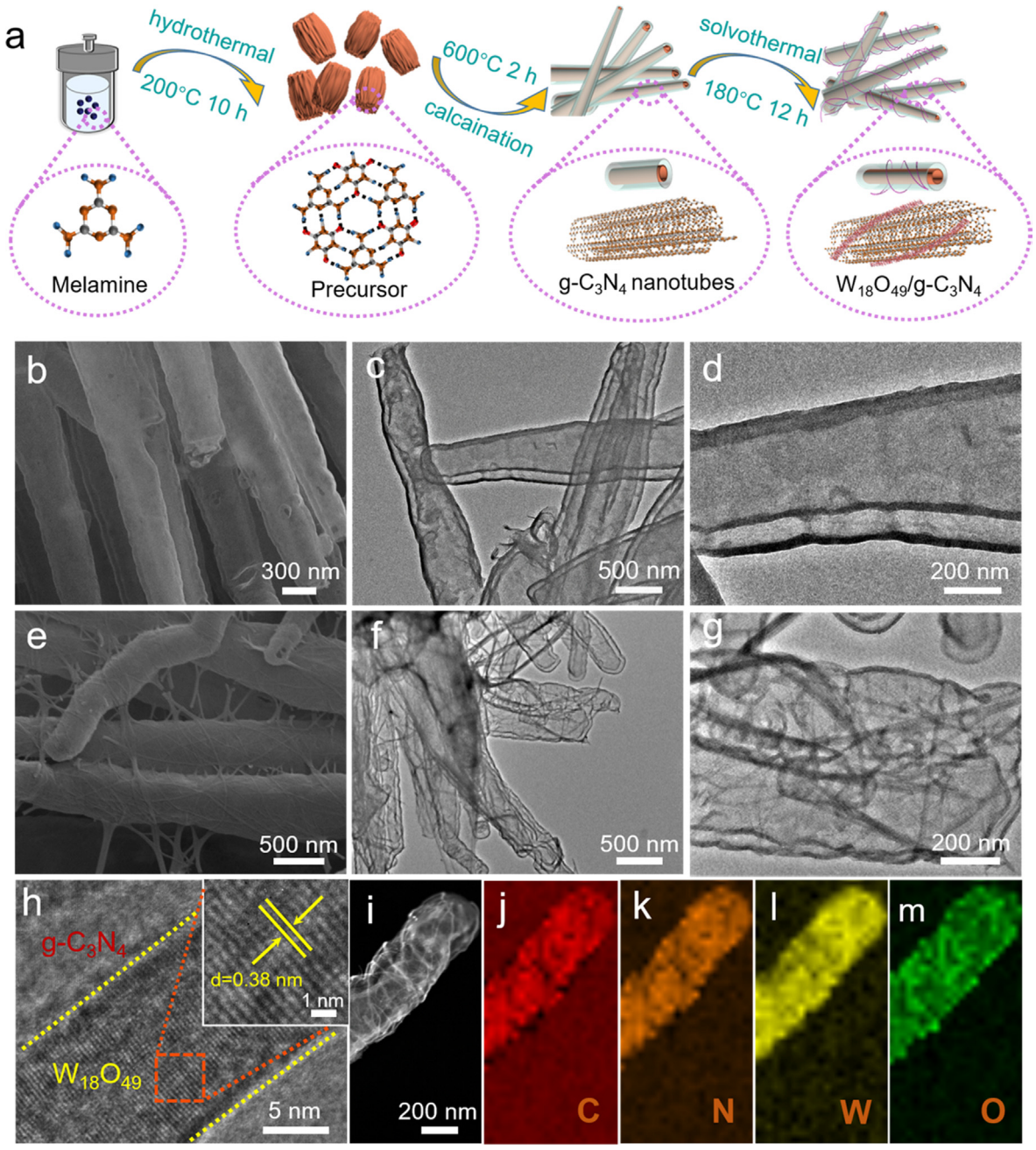

Fig. 1. (a) The synthetic route diagram of $W_{18}O_{49}$/g-C_3N_4. (b-d) The SEM and TEM images of CNNT. (e-g) The SEM and TEM images of W20-CNNT. (h) HRTEM images of W20-CNNT. (i-m) TEM and the corresponding elemental mapping images of W20-CNNT.

photocatalytic performance towards multiple applications [11]. For example, the sulfur vacancies-VS_2@C_3N_4 photocatalyst prepared by Yin et al. could facilitate the separation of electrons and holes to simultaneously boost the photocatalytic H_2 yield and the wastewater degradation ability [12]. Ong et al. successfully designed a Z-Scheme $Ag/AgVO_3$/g-C_3N_4 heterojunction photocatalyst for the photodegradation of ciprofloxacin and photocatalytic H_2 production [13]. A porous g-C_3N_4/TiO_2 S-scheme heterojunction photocatalyst synthesized by Sun et al. not only allowed the extension of the light absorption range, but also reserved outstanding redox ability [14]. The g-C_3N_4 possesses a more negative conduction band minimum (CBM) than the reduction potential of H^+/H_2 (0 V vs NHE) [15], which is considered as a promising material for photocatalytic H_2 production. Although pristine g-C_3N_4 exhibits satisfactory photocatalytic reduction ability, its low valence band maximum (VBM) usually leads to weak oxidation ability [16]. Seeking materials with matched band positions to construct g-C_3N_4-based heterojunction can endow the photoinduced carriers with stronger redox ability and higher migration rate. Additionally, non-stoichiometric semiconductors (WO_{3-x}, MoO_{3-x}, $Cu_{2-x}S$) have attracted a lot of attention because of their localized surface plasmon resonance (LSPR) effect and tunable band structure [17–19]. Unlike the plasma noble metal nanostructures, LSPR effect in these semiconductors are derived from collective oscillations of excess free carriers in lattice vacancies [18]. Among these semiconductors, tungsten oxide ($W_{18}O_{49}$) is a stable plasma semiconductor. The collective oscillations of excess free carriers associated with the abundance of oxygen vacancies in $W_{18}O_{49}$ enables the LSPR absorption in the visible and near-infrared regions (NIR), and this fascinating LSPR optical property further broadens the light absorption range [20,21]. Albeit its CBM is too low to produce H_2, its suitable VBM position delivers a strong oxidizing ability for standout photocatalytic degradation and sterilization performances [22]. Therefore, a well-designed heterojunction constructed by $W_{18}O_{49}$ and g-C_3N_4 might endow the photocatalyst with improved light utilization rate and facilitated migration kinetics of electrons and holes. A high-efficiency multifunctional photocatalysts can be obtained accordingly, but has rarely been reported at present.

Herein, an S-scheme $W_{18}O_{49}$/g-C_3N_4 heterojunction photocatalyst was developed through wrapping $W_{18}O_{49}$ nanowires (NWs) on the double-layer hollow g-C_3N_4 nanotube (CNNT). Through the finite-difference time-domain (FDTD) simulation and ultraviolet–visible (UV–vis) diffuse reflectance, the effects of the architecture of double-layer hollow nanotubes and the recombination of $W_{18}O_{49}$ NWs on the light absorption of the catalyst were analyzed in detail. The construction of S-scheme $W_{18}O_{49}$/g-C_3N_4 heterojunction reserved electrons (e^-) and holes (h^+) with strong redox ability, which promoted the separation and utilization of photogenerated carriers. Thanks to these merits, the S-scheme heterojunction photocatalyst exhibits efficient photocatalytic H_2 production, degradation and sterilization performances. Moreover, the photocatalytic mechanism was probed and analyzed by photocatalytic tests, density functional theory (DFT) calculations, electron spin resonance (ESR) measurements and trapping agent experiments.

2. Experimental section

2.1. Materials

Melamine ($C_3H_6N_6$, 99 %), tungsten chloride (WCl_6, 99.9 %), hexadecyl trimethyl ammonium bromide (CTAB, $C_{19}H_{42}BrN$, 99 %), and rhodamine B (RhB, $C_{28}H_{31}ClN_2O_3$, AR) were purchased from

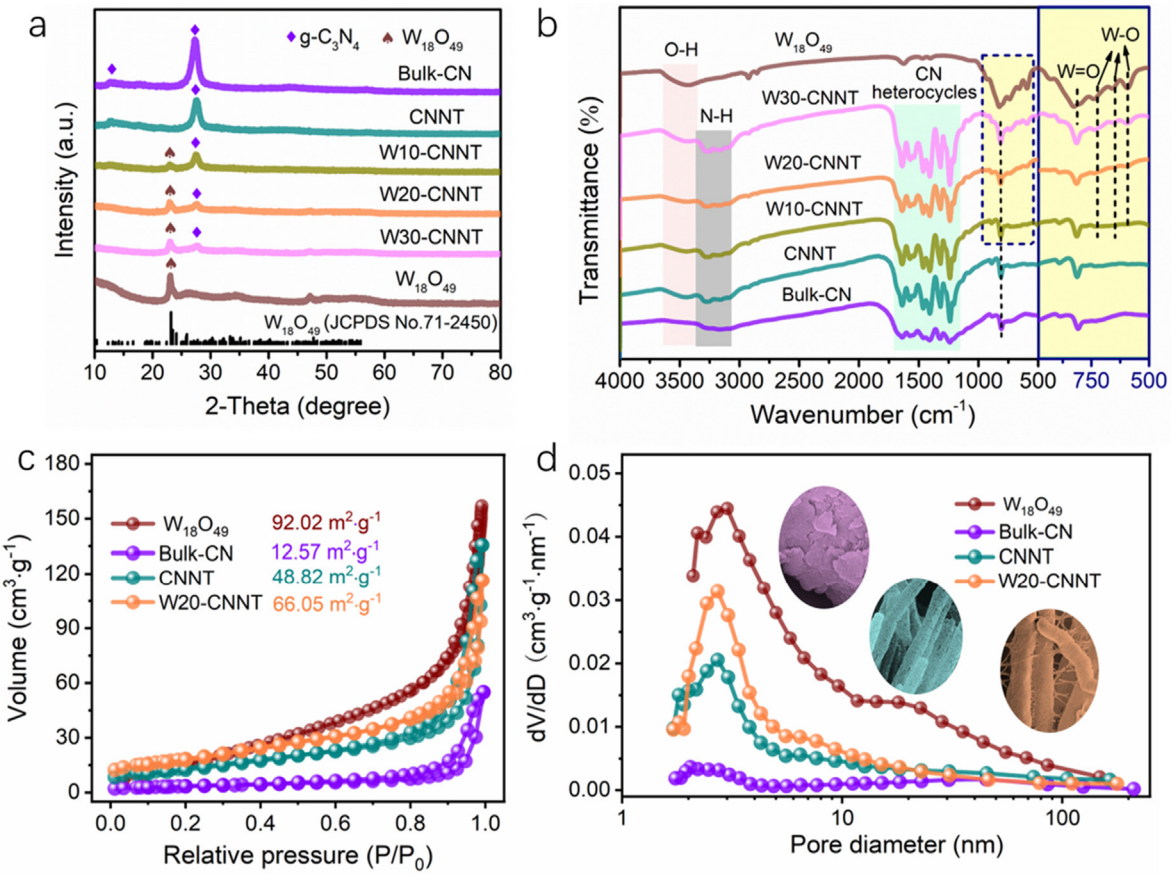

Fig. 2. (a) XRD patterns. (b) FTIR spectra. (c) N_2 adsorption–desorption isotherms. (d) The corresponding pore size distribution curves.

Aladdin Chemical Co., ltd. Nutrient agar (BR), nutrient broth (BR) and Escherichia coli (*E. coli*) were obtained from Qingdao Hope Biotechnology Co., ltd.

2.2. Synthesis of double-layer hollow g-C_3N_4 nanotube (CNNT)

0.5 g of melamine was dispersed in 60 mL of H_2O and sonicated for 15 min, and then the solution was placed in a Teflon-lined autoclave and kept at 200 °C for 10 h. After the oven was cooled to 40 °C, the reactants were collected, washed, centrifuged, and freeze-dried. The dried products were calcined at 600 °C for 2 h (2 °C/min, Ar atmosphere). Finally, the double-layer hollow g-C_3N_4 nanotubes were prepared. Under the same calcination conditions, bulk g-C_3N_4 (Bulk-CN) was obtained by direct calcination of melamine in a tube furnace.

2.3. Synthesis of $W_{18}O_{49}$/g-C_3N_4 hybrid

$W_{18}O_{49}$ NWs-modified CNNT was synthesized by a solvothermal method on the basis of our previous work [23]. 80 mg of the as-prepared CNNT and 1 mg of CTAB were dispersed in 25 mL ethanol by ultrasound and stirring. Then different amounts of WCl_6 were added to the above suspension. After stirring for 30 min. the mixture was placed in an oven and heated at 180 °C for 12 h. Finally, the $W_{18}O_{49}$/g-C_3N_4 composite was gained after centrifugation, washing and drying. According to the added amounts of WCl_6 (10, 20, and 30 mg), the as-prepared samples were labeled as W10-CNNT, W20-CNNT, and W30-CNNT, respectively.

2.4. Characterization

The crystal phase properties were tested by X-ray diffraction (XRD) with Cu Kα radiation (Bruker D8 Advance). The morphology characteristics were observed by a ZEISS SUPRA55 field emission scanning electron microscope (FESEM) and a FEI Tecnai G2 S-Twin transmission electron microscope (HRTEM) equipped with X-ray energy dispersive spectroscopy (EDS). The chemical states and compositions were analyzed using a Thermo Scientific ESCALAB 250Xi X-ray photoelectron spectroscopy (XPS) and a Nicolet iS5 Fourier transform infrared spectra (FTIR). The photoluminescence spectra (PL) and diffuse reflectance spectra (DRS) were measured using a fluorescence spectrometer (HORIBA FluoroMax-4) and a HITACHI UH-4150 UV–vis spectrometer, respectively. Brunauer, Emmett and Teller (BET) specific surface area was carried out on an ASAP 2460 Micromeritics Tristar II. Electron spin resonance (ESR) was tested with a Bruker electron spin resonance spectrometer. 5, 5-dimethyl-1-pyrroline-*N*-oxide (DMPO) served as a sacrificial agent for $\cdot O_2^-$ and ·OH. The photocurrent response and electrochemical impedance (EIS) curves were recorded by an Autolab PGSTAT302N electrochemical workstation.

2.5. Photocatalytic H_2 evolution

10 mg of catalyst was dispersed in a solution containing 45 mL of H_2O, 5 mL of triethanolamine and a certain amount of H_2PtCl_6 solution (3 wt% Pt). The photocatalytic H_2 evolution reaction was carried out in a sealed quartz reactor. In the process of photocat-

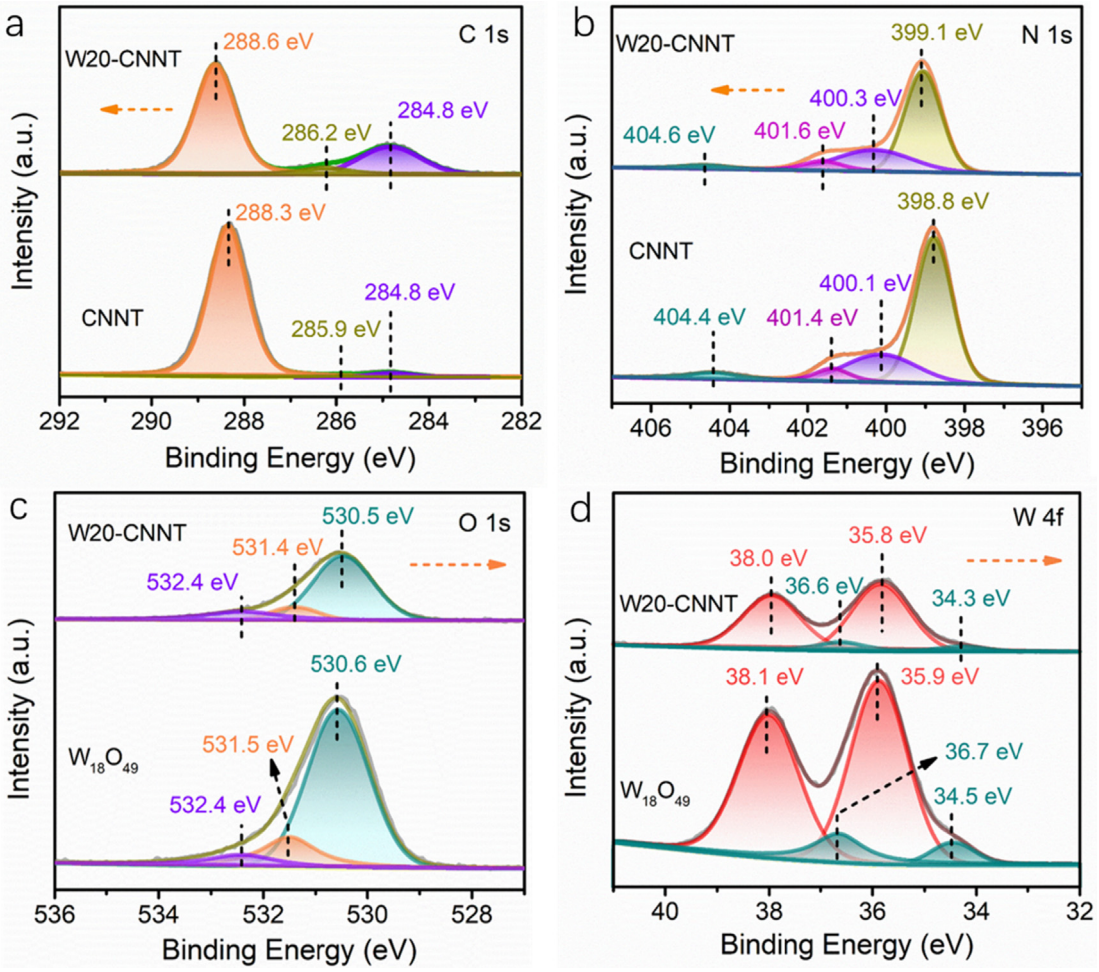

Fig. 3. XPS spectra of samples: (a) C 1 s spectra; (b) N 1 s spectra; (c) O 1 s spectra; (d) W 4f spectra.

alytic H_2 production, a 300 W Xe lamp ($\lambda \geq 420$ nm) was used as the light source, and the temperature of the reaction vessel was maintained at 6 °C. The generated H_2 was detected by gas chromatography (GC-7920, Beijing China Education Au-light Technology Co., ltd.). The apparent quantum efficiency (AQE) was calculated using the equation (1):

$$\text{AQE}\ (\%) = \frac{N_e}{N_p} \times 100\% \quad (1)$$

Here N_e and N_p were the amounts of reaction electrons and incident photons, respectively.

2.6. Photocatalytic degradation performance

10 mg of catalyst was dispersed into 50 mL of RhB solution (10 mg·L^{-1}). The above suspension was placed in the dark environment and stirred for 30 min before light irradiation (300 W Xe lamp, $\lambda \geq 420$ nm) to achieve the adsorption–desorption equilibrium. Then 5 mL of suspension was taken out at intervals of 3 min under light irradiation and the catalyst was removed by centrifugation. The concentration of RhB was tested by a UV–vis spectrophotometer (HITACHI UH-5300).

2.7. Photocatalytic sterilization performance

Before the experiments, the required equipment and the culture medium solution were autoclaved (121 °C, 15 min) for use. Preparation of nutrient agar solid medium: 20 g of agar was heated and dissolved in 500 mL of H_2O. After steam sterilization, agar liquid medium was cooled to 60–70 °C, then poured into petri dishes and solidified. Preparation of nutrient broth liquid medium: 0.9 g of nutrient broth powder was dissolved in 50 mL of H_2O under heating. Preparation of bacterial solution: An appropriate amount of *E. coli* strains was inoculated into 50 mL of sterilized nutrient broth liquid medium and cultured at 37 °C for 18 h to obtain *E. coli* suspension. 50 μL of cultured *E. coli* suspension was added to 50 mL of 0.9 % (w/v) normal saline, and the bacterial concentration in the solution was about 10^{10} CFU/mL. The concentration of the bacterial solution in the sterilization experiment was 10^7 CFU/mL, which was adjusted by gradient dilution method using normal saline.

In the photocatalytic sterilization experiment, the change of the number of active strains with illumination time was detected by dilution plate coating method. Photocatalytic bacteriostatic test: Typically, 10 mg of catalyst was added to 50 mL of bacterial solu-

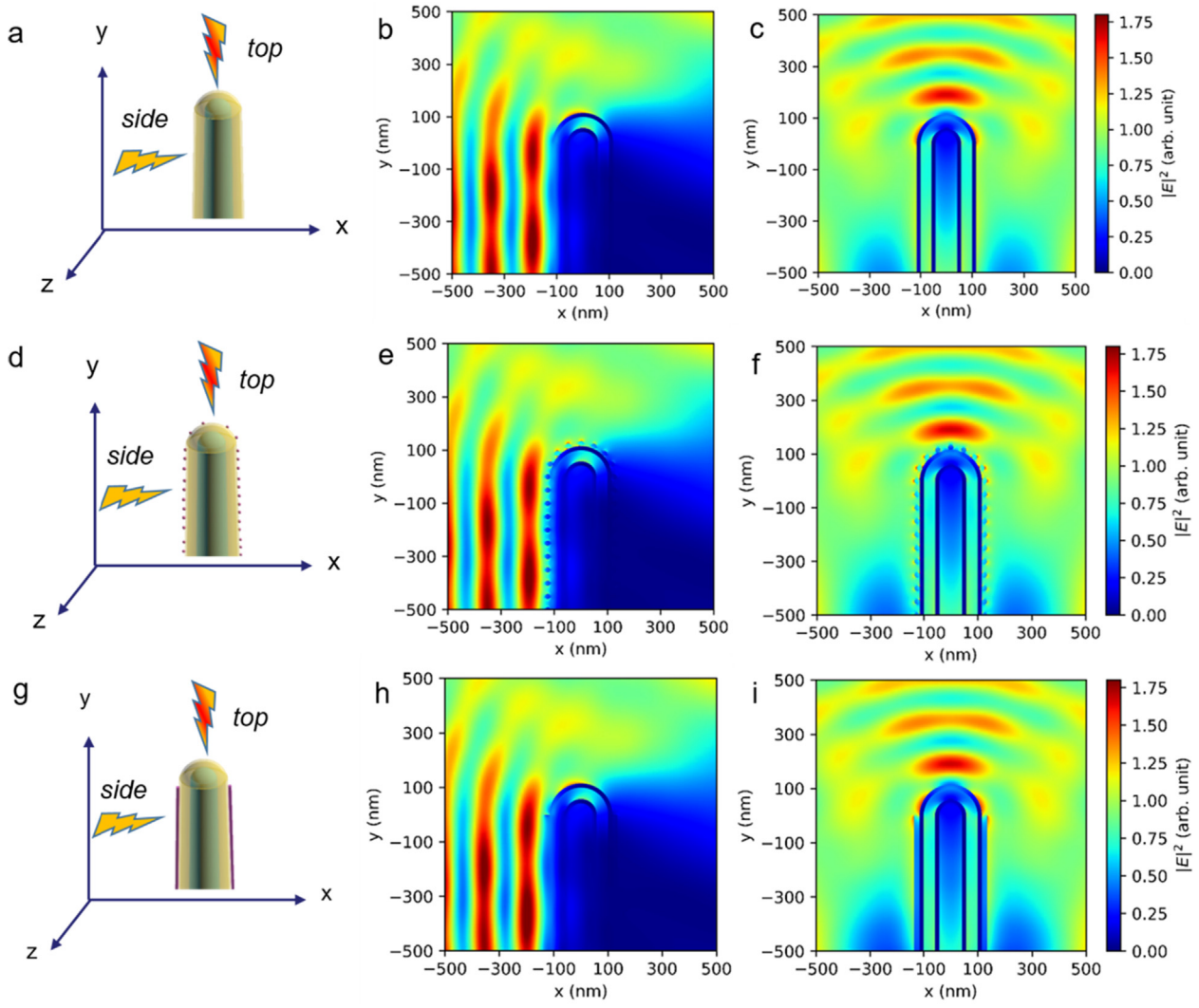

Fig. 4. The simplified structure models and the corresponding FDTD simulated electric field distribution at the center section (xy plane, 420 nm). (a) g-C_3N_4 nanotube; (b) g-C_3N_4 nanotube, side; (c) g-C_3N_4 nanotube, top; (d) perpendicular, $W_{18}O_{49}$/g-C_3N_4; (e) perpendicular, $W_{18}O_{49}$/g-C_3N_4, side; (f) perpendicular, $W_{18}O_{49}$/g-C_3N_4, top; (g) parallel, $W_{18}O_{49}$/g-C_3N_4; (e) parallel, $W_{18}O_{49}$/g-C_3N_4, side; (f) parallel, $W_{18}O_{49}$/g-C_3N_4, top.

tion (10^7 CFU/mL). At given irradiation (300 W Xe lamp, $\lambda \geq 420$ nm) time interval (0, 10, 20, 30 min), 100 μL of suspension was spread on solid medium. After incubating at 37 °C for 18 h, the number of surviving bacteria colonies was counted. Two parallel experiments were carried out each time to reduce experimental error. Control experiment (only visible light without catalyst) was also performed.

2.8. The finite-difference time-domain (FDTD) method

The optical field intensities under plane waves illumination were calculated with a 2-dimensional finite-difference time-domain (2D FDTD) simulation (Lumerical FDTD Solutions). The background refractive index was set as the refractive index of water. The simulation area was surrounded by Perfect absorbing layers (PML), so that unwanted reflections were eliminated.

2.9. Density functional theory (DFT) calculation

All DFT calculations were performed using the Vienna *ab initio* simulation package (VASP) The Perdew-Burke-Ernzerhof (PBE) function of the Generalized Gradient Approximation (GGA) was used to describe the exchange–correlation energy. To describe the expansion of the electronic eigenfunctions, the projector-augmented wave (PAW) method was applied with a kinetic energy cutoff of 500 eV. The total energy and force convergence threshold were set to 10^{-6} eV and 0.02 eV $Å^{-1}$, respectively. The Brillouin zone was sampled with a 4 × 4 × 1 k-point grid of the Monkhorst-Pack scheme. A 15 Å vacuum was set above slabs to avoid interaction between the two periodic images.

3. Results and discussion

3.1. Synthesis diagram and morphology analysis

The synthesis schematic of $W_{18}O_{49}$/g-C_3N_4 was shown in Fig. 1a. The fusiform-like precursors were obtained by hydrothermal process of melamine (Fig. S1). Note that double-layer hollow g-C_3N_4 nanotube (CNNT) were obtained after the calcination of the precursor (Fig. 1b-d). These nanotubes with diameters ranging from 500 to 700 nm have a wall thickness of ~ 25 nm. After the solvothermal process of CNNT in WCl_6 ethanol solution, the $W_{18}O_{49}$/g-C_3N_4 composite was constructed by winding $W_{18}O_{49}$ NWs on CNNT (Fig. 1e-g, Fig. S2). The diameter of these twining nanowires was approximately 15 nm. In the HRTEM image of the W20-CNNT composite (Fig. 1h), clear lattice fringes with a lattice spacing of about

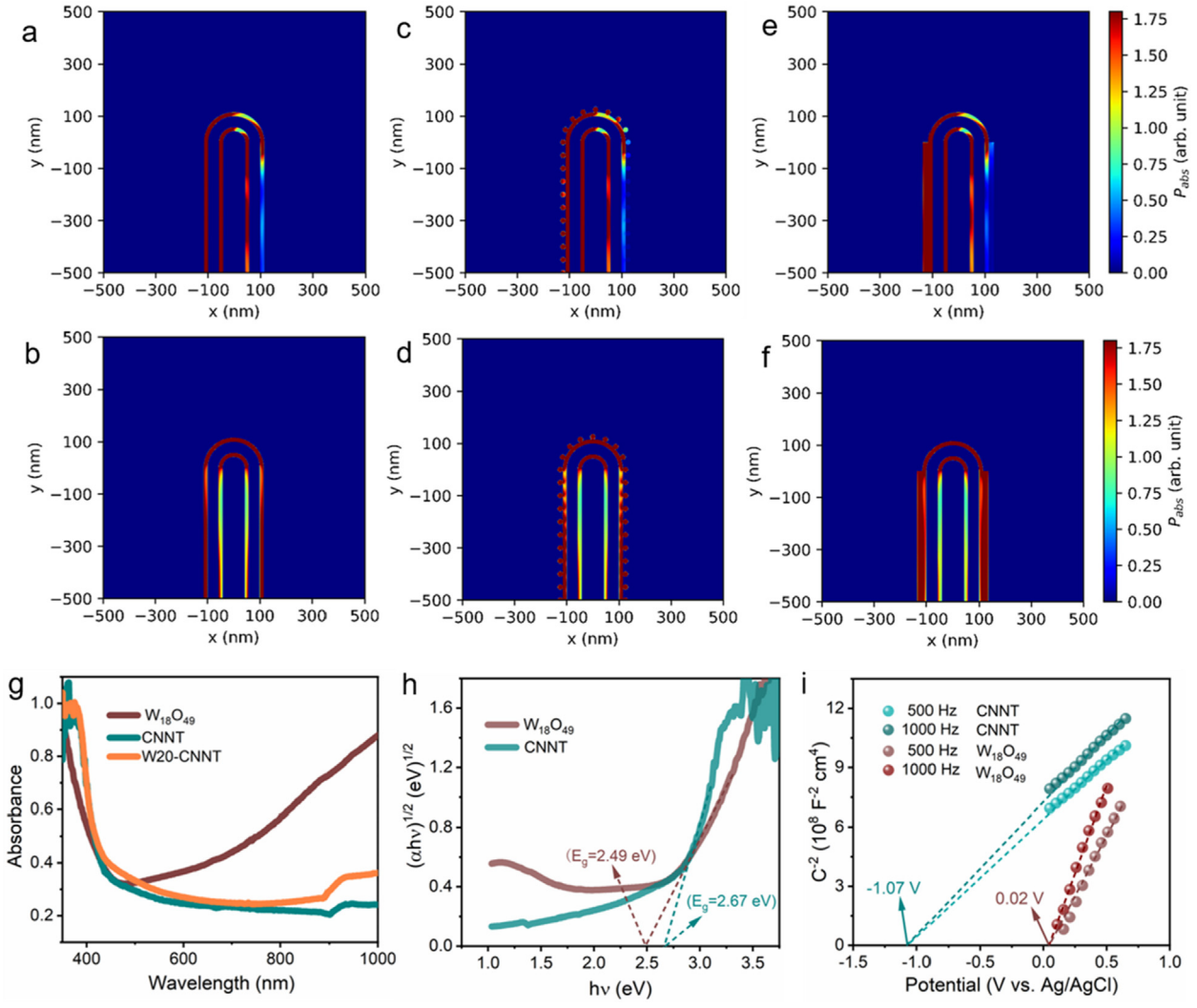

Fig. 5. Optical absorption intensity distribution in x-y plane (420 nm). (a) g-C_3N_4 nanotube, side; (b) g-C_3N_4 nanotube, top; (c) perpendicular, $W_{18}O_{49}$/g-C_3N_4, side; (d) perpendicular, $W_{18}O_{49}$/g-C_3N_4, top; (e) parallel, $W_{18}O_{49}$/g-C_3N_4, side; (f) parallel, $W_{18}O_{49}$/g-C_3N_4, top. (g) UV–vis DRS spectra, (h) band gap, and (i) Mott-Schottky plots.

0.38 nm could be observed, corresponding to the (010) crystal plane of monoclinic $W_{18}O_{49}$ [24], which indicated that $W_{18}O_{49}$ was successfully compounded on CNNT. In SEM and TEM images of W10-CNNT and W30-CNNT (Fig. S2), $W_{18}O_{49}$ NWs assembled on CNNT could also be discovered. The elemental mapping images of W20-CNNT showed uniform distributions of W and O elements on the surface of CNNT (Fig. 1i-m). The SEM, TEM and HRTEM images of $W_{18}O_{49}$ NWs were presented in Fig. S3, which was approximately 20 nm in diameter. The actual elemental ratios of different samples were provided in the EDS (Fig. S4). In addition, the SEM image of W20-CNNT prepared without the addition of CTAB was shown in Fig. S5. Irregular Bulk-CN was obtained by direct calcination of melamine (Fig. S6).

3.2. Structure and composition of the photocatalysts

There are two diffraction peaks at 2θ = 12.8° and 27.4° in the XRD patterns of Bulk-CN and CNNT (Fig. 2a), representing that the in-plane structural repeating units and interplanar stacking of aromatic systems in g-C_3N_4. The diffraction peaks of $W_{18}O_{49}$ NWs are consistent with those of monoclinic phase $W_{18}O_{49}$ (JCPDS No. 71–2450) [25]. The diffraction peaks of $W_{18}O_{49}$ and g-C_3N_4 can be observed in the $W_{18}O_{49}$/g-C_3N_4 hybrid. Meanwhile, the diffraction peak intensity of $W_{18}O_{49}$ (010) crystal plane at 2θ = 23.3° gradually strengthened with the increase composite amount of $W_{18}O_{49}$, all of which demonstrated that $W_{18}O_{49}$ NWs were successfully anchored on CNNT. In FTIR spectra (Fig. 2b), the peaks at 3000–3650 cm^{-1} are assignable to the vibration modes of N—H in the uncondensed amino groups and O—H in adsorbed water molecules [26]. The breathing mode of the triazine units and the stretching vibration of the CN heterocyclic ring are located at 810 cm^{-1} and 1160–1700 cm^{-1}, respectively [27]. The peaks at 812, 724, 647, and 595 cm^{-1} in W10-CNNT, W20-CNNT and W30-CNNT are indexed to the stretching vibration of W = O and W-O bonds [28], and their intensity strengthens with the increase of $W_{18}O_{49}$ amount. This is in agreement with the results observed in XRD. The FTIR spectrum of the fusiform-like precursor was provided in Fig. S7. The specific surface areas of $W_{18}O_{49}$, Bulk-CN, CNNT and W20-CNNT are 92.02, 12.57, 48.82 and 66.05 $m^2 \cdot g^{-1}$, respectively (Fig. 2c, Table S1). The specific surface area of double-layer hollow g-C_3N_4 nanotube (CNNT) is higher than that of bulk g-C_3N_4 (Bulk-CN), and the specific surface area of W20-CNNT loaded with $W_{18}O_{49}$ nanowires is further increased. Obviously, the construction of the double-layer hollow nanotubes and the decoration of $W_{18}O_{49}$ NWs dramatically increased the specific surface area. Moreover, the pore size mainly concentrated at 2–4 nm in these samples (Fig. 2d), suggesting the mesoporous structure. This might promote the transport and transfer of reactant molecules to enhance the catalytic performances.

The chemical composition and state of samples were further analyzed by XPS. The peaks of W, O, C and N elements could be observed in the XPS full survey spectrum of W20-CNNT (Fig. S8). The peaks around 284.8, 285.9 and 288.3 eV in the C 1 s spectra (Fig. 3a) were ascribed to exogenous carbon, C-NH_x, and sp^2

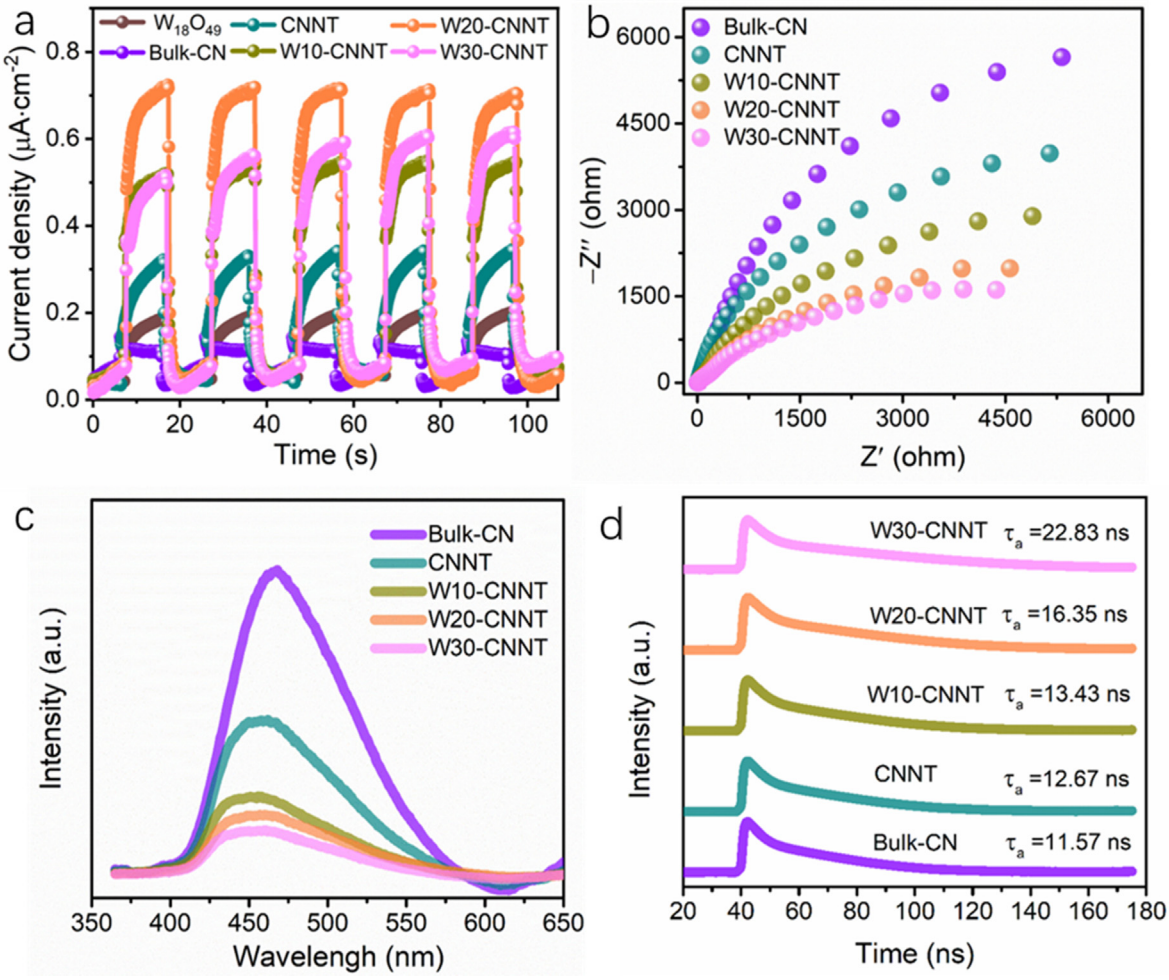

Fig. 6. (a) Photocurrent response, (b) EIS curves, (c) PL spectra and (d) time-resolved transient PL decay spectra of different samples.

hybridized N-C═N, respectively [4]. The N 1 s spectra (Fig. 3b) could be de-convoluted into four peaks, corresponding to charge polarization (404.4 eV), C-NH_x (401.4 eV), N-C_3 (400.1 eV), C-N═C (398.8 eV), respectively [29]. The peaks at 530.6, 531.5 and 532.4 eV in O 1 s spectra (Fig. 3c) were dedicated to lattice oxygen, oxygen vacancy and surface adsorbed oxygen, respectively [30]. In the W 4f spectra (Fig. 3d), the characteristic peaks at approximately 35.9 and 38.1 eV represented W^{6+}, while those at 34.5 and 36.7 eV symbolized W^{5+} [25]. It was remarkable that the peaks of C 1 s and N 1 s in W20-CNNT shifted to higher binding energy compared with the peak positions of pristine CNNT and $W_{18}O_{49}$, while the peaks of W 4f and O 1 s shifted toward lower binding energy. This implies the interfacial interaction between $W_{18}O_{49}$ and g-C_3N_4, and electrons might be transferred from g-C_3N_4 to $W_{18}O_{49}$ [31].

3.3. Optical absorption analysis

The current reports on photocatalysts mainly focus on the exploration of photo-electric separation efficiency and surface reactions of catalyst. There are few studies on the light-induced electric field and light absorption intensity, and most of them stay in the study of the light absorption range. The changes of catalyst morphologies and material characteristics can affect the light

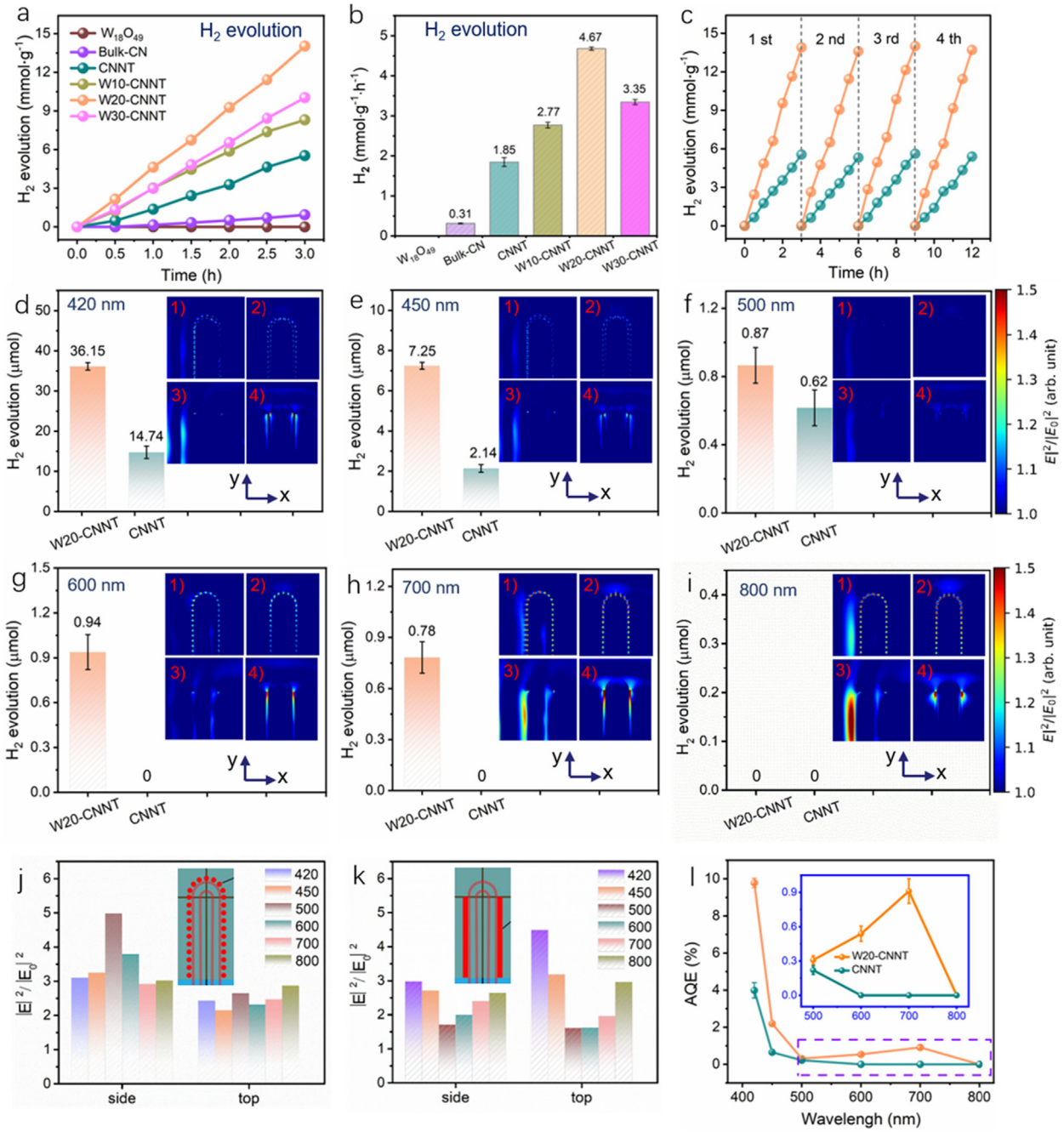

Fig. 7. (a,b) Photocatalytic H_2 evolution performances ($\lambda \geq 420$ nm). (c) Stability tests of CNNT (cyan) and W20-CNNT (orange). (d-i) Photocatalytic H_2 evolution amounts (irradiating for 1 h) and (insets) the electric field enhancement distribution of $W_{18}O_{49}$/g-C_3N_4 in xy plane relative to g-C_3N_4 nanotube under different wavelengths. Insets: 1) perpendicular, side; 2) perpendicular, top; 3) parallel, side; 4) parallel, top. The maximum electric field enhancement factors of the $W_{18}O_{49}$/g-C_3N_4 heterostructure: (j) perpendicular; (k) parallel. (l) AQE of W20-CNNT and CNNT under different wavelengths. The above error bars were calculated via repeating the tests for three times.

absorption properties [32]. The FDTD method was adopted to investigate the light absorption characteristics of photocatalyst (Fig. S9) [33–35]. Note that for $W_{18}O_{49}$/g-C_3N_4 hybrid, $W_{18}O_{49}$ NWs are wound on the surface of double-layer hollow g-C_3N_4 nanotubes. From a physical point of view, this situation can be modeled as two cases: (1) $W_{18}O_{49}$ NWs are perpendicular to hollow nanotubes; (2) $W_{18}O_{49}$ NWs are parallel to hollow nanotubes. Therefore, both cases were simulated for $W_{18}O_{49}$/g-C_3N_4. FDTD simulation results manifest that the light can penetrate the interior of the cavity and generate a localized electric field at the edge and inside of the cavity structure for the double-layer hollow g-C_3N_4 nanotube, whether it is irradiated from the side or from the top (Fig. 4a-c, Fig. S10). Furthermore, when $W_{18}O_{49}$ NWs were adhered to the surface of g-C_3N_4 nanotube, the electric filed intensity at the edge of the cavity was further enhanced (Fig. 4d-i, Fig. S11, and Fig. S12).

The electric field distribution results only represent the distribution of light intensity. The light absorption analysis is more important for photocatalysts. Therefore, the light absorption intensity distribution was calculated according to the electric field distribution results [36]. For different incident wavelengths, the light absorption intensity at the edge of $W_{18}O_{49}$/g-C_3N_4 is stronger than that of g-C_3N_4 nanotube (Fig. 5a-f, Fig. S13-15), indicating that the $W_{18}O_{49}$ NWs on the surface of g-C_3N_4 nanotube can enhance the light absorption. $W_{18}O_{49}$ has a wide light absorption range in the UV–vis-NIR region as reflected in the DRS spectra (Fig. 5g), which might originate from the LSPR effect. Moreover, W20-CNNT also exhibited weak absorption in the NIR region due to the loading of a small amount of $W_{18}O_{49}$. According to the FDTD simulation results and UV–vis diffuse reflectance spectra, the improvement in the light absorption capacity (including the light absorption range and intensity) for $W_{18}O_{49}$/g-C_3N_4 can be considered as the synergistic effect of the double-layer hollow nanotube structure and the $W_{18}O_{49}$ NWs. The band gaps of CNNT and $W_{18}O_{49}$ are approximately 2.67 and 2.49 eV, respectively (Fig. 5h). The flat band positions of CNNT and $W_{18}O_{49}$ measured by the Mott-Schottky plots were − 1.07 and 0.02 V (vs Ag/AgCl), respectively (Fig. 5i), corresponding to − 0.87 and 0.22 V (vs NHE), which can be regarded as the conduction band position of *n*-type semiconductor [37,38]. Based on their band gaps, the valence band positions of CNNT and $W_{18}O_{49}$ are 1.80 and 2.71 eV, respectively, which are similar to the results obtained by the XPS valence band spectra (Fig. S16).

3.4. Carriers separation efficiency analysis

The separation and transfer behaviors of the photogenerated carriers were investigated. Compared with pristine Bulk-CN and CNNT, the higher photocurrent densities in W10-CNNT, W20-CNNT and W30-CNNT suggested that the $W_{18}O_{49}$/g-C_3N_4 heterojunction photocatalysts possessed higher photogenerated electron-hole separation rates (Fig. 6a) [39]. In the EIS curves (Fig. 6b), the smaller arc radius indicated that they displayed faster charge transfer rates [40]. Furthermore, W10-CNNT, W20-CNNT and W30-CNNT exhibited lower fluorescence intensity than pure g-C_3N_4 (Fig. 6c). This revealed that the construction of heterojunction could inhibit the recombination of photogenerated electron-hole [41]. Their longer fluorescence lifetimes illustrated that more photogenerated carriers could participate in subsequent photocatalytic reactions (Fig. 6d and Table S2) [42]. The above results proved that $W_{18}O_{49}$/g-C_3N_4 heterojunction rendered facilitated separation and transport rates of photogenerated electron-hole compared with pristine g-C_3N_4. This will play a critical role in promoting the photocatalytic performance towards multiple applications.

3.5. Photocatalytic performances tests

The photocatalytic H_2 evolution tests were conducted under visible light irradiation. The H_2 evolution rate of CNNT is approximately 5.97 times that of Bulk-CN, while $W_{18}O_{49}$ NWs have no photocatalytic H_2 evolution ability (Fig. 7a,b). However, when $W_{18}O_{49}$ NWs were decorated on CNNT, the H_2 evolution rates of $W_{18}O_{49}$/g-C_3N_4 (W10-CNNT, W20-CNNT, and W30-CNNT) were remarkably enhanced. Thereinto, W20-CNNT reached a high H_2 evolution rate of 4.67 mmol·g^{-1}·h^{-1}, which was approximately 15.1 times that of Bulk-CN and outperformed many other reported

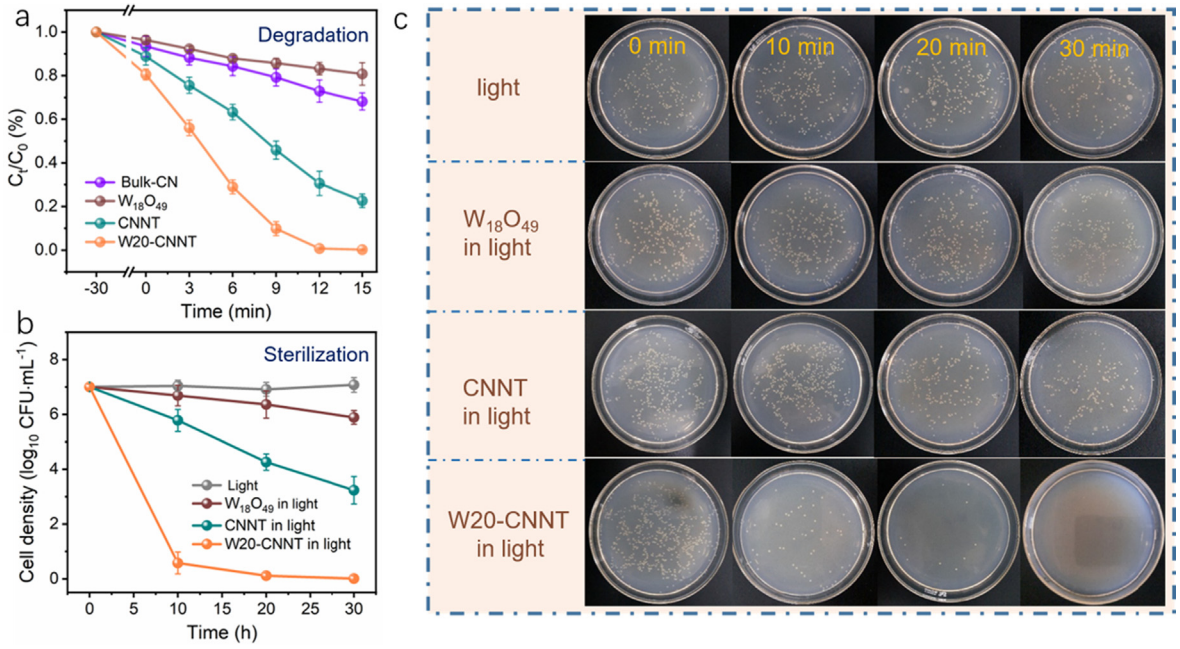

Fig. 8. (a) Photocatalytic degradation curves of catalysts for RhB ($\lambda \geq 420$ nm). The error bars were calculated via repeating the tests for three times. (b) Photocatalytic antibacterial tests ($\lambda \geq 420$ nm). Two parallel experiments were carried out each time. (c) The growth of *E. coli* colonies under different conditions.

catalysts (Table S3). Moreover, W20-CNNT exhibited outstanding photocatalytic cycle stability (Fig. 7c). The TEM images and XRD pattern of W20-CNNT after photocatalytic test also proved its satisfactory stability (Fig. S17). The photocatalytic H_2 evolution amounts of W20-CNNT and CNNT were evaluated under different light wavelengths (Fig. 7d-i). The results showed that the H_2 production amount of W20-CNNT was higher than that of CNNT under 420, 450, and 500 nm light irradiation. Surprisingly, W20-CNNT could still produce H_2 under the illumination of 600 and 700 nm wavelength, while CNNT failed at the same conditions. To further analyze the effect of $W_{18}O_{49}$ on the photocatalytic H_2 evolution performance in terms of optical properties, the electric field enhancement distribution of $W_{18}O_{49}$/g-C_3N_4 relative to g-C_3N_4 nanotube at different wavelengths was simulated [43]. From the simulated electric field enhancement distribution and the obtained enhancement factor (Insets of Fig. 7d-i, Fig. 7j,k), the local electric field intensity of $W_{18}O_{49}$/g-C_3N_4 is stronger than that of g-C_3N_4 nanotube at different wavelengths. Considering the optical properties of $W_{18}O_{49}$, the reasons for the improved H_2 production performance of $W_{18}O_{49}$/g-C_3N_4 were further analyzed. On the one hand, the decoration of $W_{18}O_{49}$ NWs on the surface of g-C_3N_4 nanotube can enhance the intensities of both local electric field and optical absorption. On the other hand, W20-CNNT still enables photocatalytic H_2 production at 600 and 700 nm, probably because the LSPR excitation of $W_{18}O_{49}$ NWs can generate strong the local electric field to form plasmonic "hot electrons" [18,44]. When these "hot electrons" were filled at the plasmon energy level higher than the CB position of g-C_3N_4, they could facilitate the photocatalytic reduction of protons at the active sites of g-C_3N_4 nanotube to generate H_2 [45]. W20-CNNT had no H_2 production performance under 800 nm wavelength illumination. This may be because the low energy/density LSPR-excitation at 800 nm wavelength is difficult to induce "hot electron" injection into the plasmon energy level higher than the CB position of g-C_3N_4, resulting in the inability of

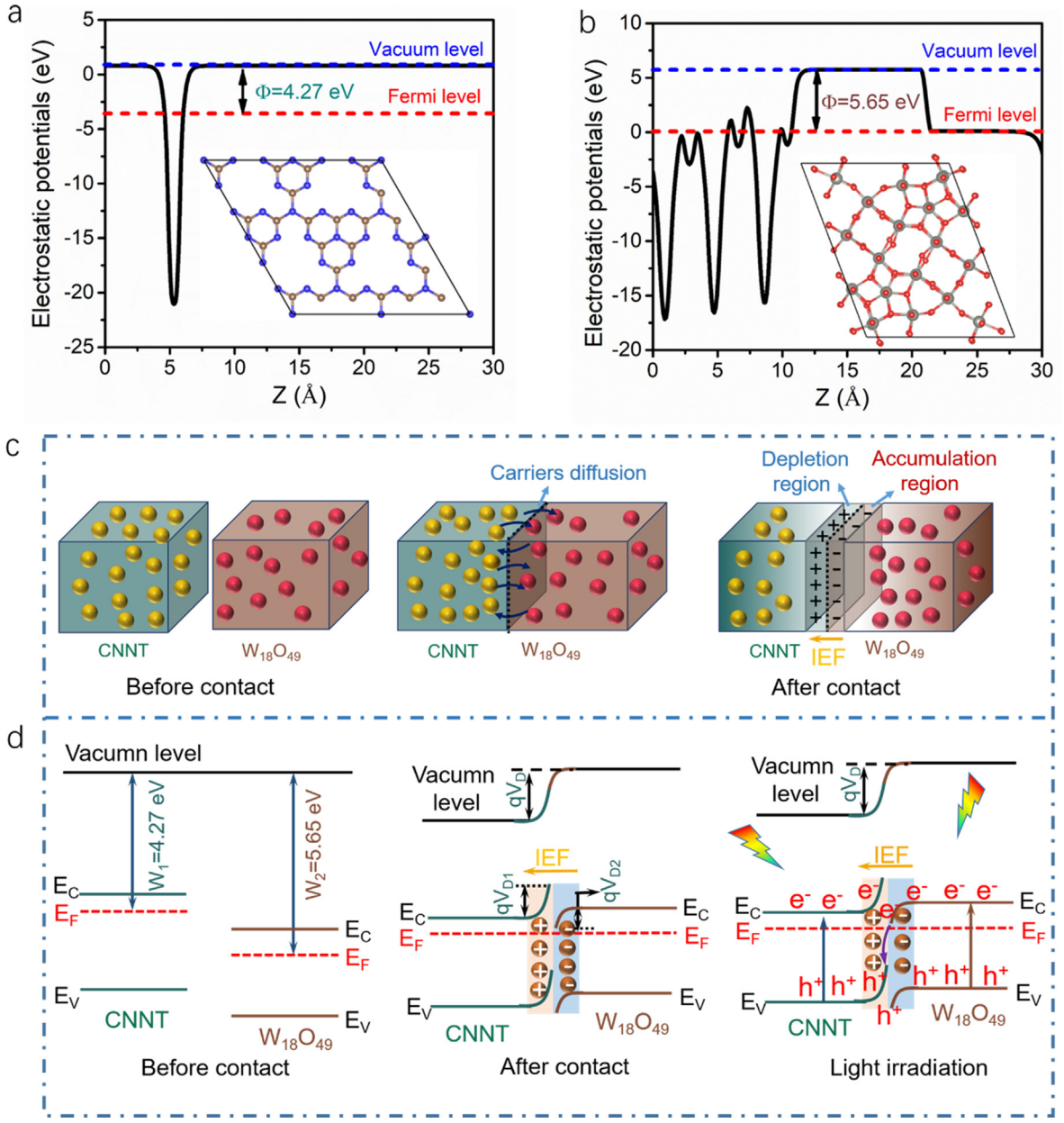

Fig. 9. Calculated work functions of (a) g-C_3N_4 and (b) $W_{18}O_{49}$. (c) Schematic diagram of carrier diffusion and injection before and after contact between $W_{18}O_{49}$ and g-C_3N_4. (d) Schematic illustration of the formation of S-scheme $W_{18}O_{49}$/g-C_3N_4 heterojunction.

these "hot electron" to transfer into the CB of g-C_3N_4, thus failing to perform photocatalytic reduction of protons [24]. The AQE of W20-CNNT and CNNT were manifested in Fig. 7l. Combined with the above analysis, although W20-CNNT exhibited photocatalytic H_2 production performance under illumination at 600–700 nm wavelength due to the LSPR effect of $W_{18}O_{49}$, its H_2 production amount is very small. The photocatalytic H_2 production performance of W20-CNNT mainly relies on light with a wavelength of 420–500 nm, which is consistent with the analysis results of UV–vis DRS spectra (Fig. 5g).

In order to verify its multifunctional photocatalytic applications, the degradation of RhB and bactericidal tests were also investigated. The degradation efficiencies of Bulk-CN, $W_{18}O_{49}$, CNNT and W20-CNNT within 12 min are 27.10 %, 16.77 %, 69.42 % and 100.00 %, respectively (Fig. 8a). This indicated that the as-designed heterojunction photocatalyst also favors photodegradation. The pseudo-first-order kinetic curves were displayed in Fig. S18, and the higher reaction rate constant in W20-CNNT also certified a faster photocatalytic degradation rate (Table S4). In addition, from the growth of *E. coli* under different conditions, visible light itself has no bactericidal performance against *E. coli* (Fig. 8b,c). When both visible light and catalyst existed, the bactericidal efficiency of $W_{18}O_{49}$, CNNT and W20-CNNT reached 9.14 %, 39.13 % and 99.41 % within 20 min, respectively (Fig. 8b,c, Fig. S19). Surprisingly, the bactericidal efficiency of W20-CNNT achieved 91.74 % in only 10 min. On the basis of the above photocatalytic tests, $W_{18}O_{49}$/g-C_3N_4 heterojunction revealed more excellent photocatalytic H_2 production, degradation and sterilization performances, which can be used as a "one stone, three birds" multifunctional photocatalyst.

3.6. Photocatalytic mechanism analysis

To investigate the transfer circumstance of carriers in $W_{18}O_{49}$/g-C_3N_4 heterojunction, the work functions of $W_{18}O_{49}$ and g-C_3N_4 were calculated to be 5.65 and 4.27 eV (Fig. 9a,b), respectively, manifesting that the Fermi energy level of g-C_3N_4 was higher than that of $W_{18}O_{49}$. When constructed as a heterojunction, the carriers near the contact interface diffuse and electrons tend to flow from g-C_3N_4 (high Fermi level) to $W_{18}O_{49}$ (low Fermi level) until the Fermi level reaches equilibrium [46]. At this time, the electron accumulation layer and depletion layer are generated at the interface, forming the built-in electric field (IEF) and producing band bending (Fig. 9c,d) [47]. The direction of electron transfer is in accordance with the XPS analysis results. The band edge of g-C_3N_4 was bent upward (barrier height qV_{D1}) and that of $W_{18}O_{49}$ was bent downward (barrier height qV_{D2}) [48]. When illuminated, the electrons of the semiconductors were excited to conduction band. Due to the influences of band bending and built-in electric field, the electrons in the CB of $W_{18}O_{49}$ tended to recombine with the holes in the VB of g-C_3N_4 to form an S-scheme heterojunction. The carrier transfer mechanism of S-scheme heterojunction not only promotes charge separation, but also preserves electrons

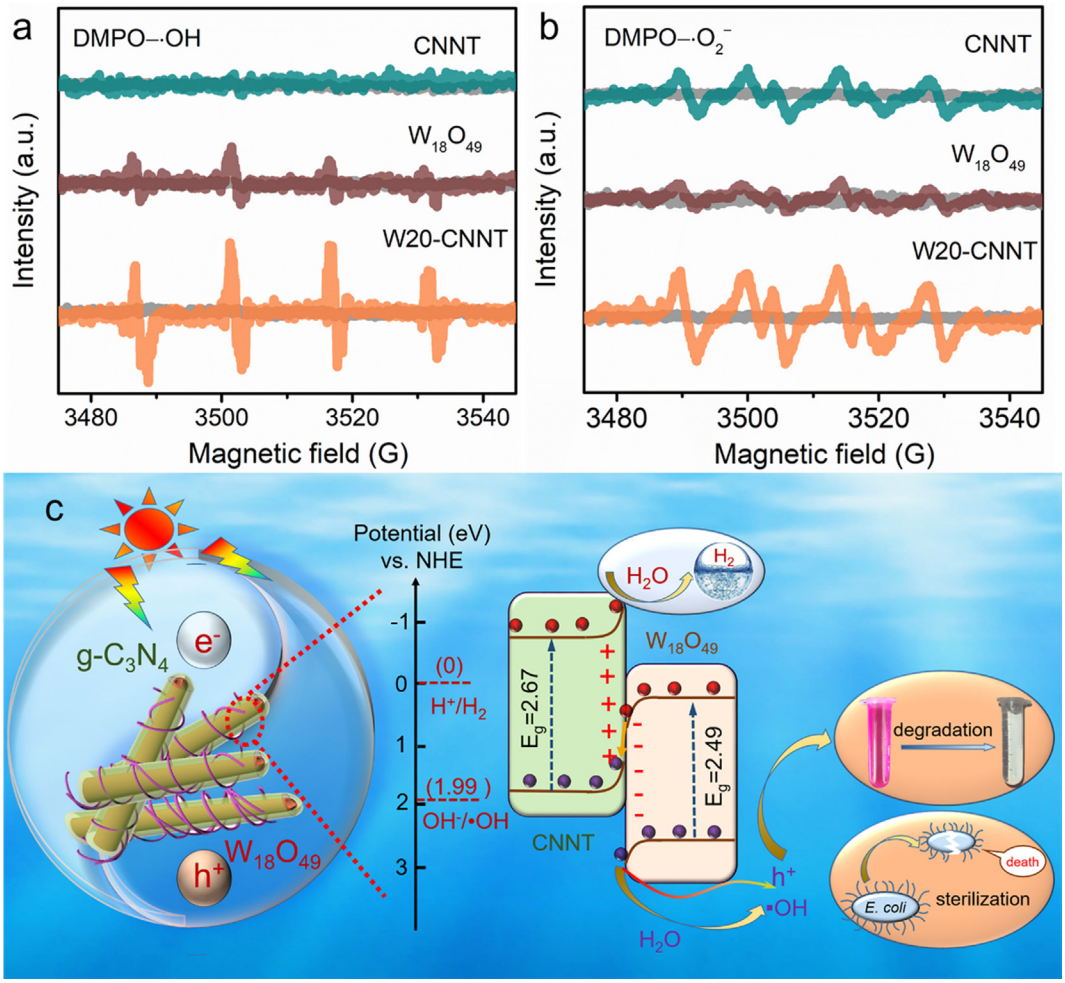

Fig. 10. ESR spectra of (a) DMPO-·OH and (b) DMPO-·O_2^- for different samples. (c) Schematic diagram of the photocatalytic mechanism.

(from g-C_3N_4) and holes (from $W_{18}O_{49}$) with higher redox ability, which might be beneficial for the multifunctional catalytic effect.

To gain the in-depth insight of the photocatalytic mechanism, the active radicals generated by the $W_{18}O_{49}$, CNNT and W20-CNNT were identified by ESR tests. DMPO, as a radical trapping agent, could react with the generated free radicals ($\cdot O_2^-$ and ·OH) to form spin adducts (DMPO-$\cdot O_2^-$ and DMPO-·OH), displaying ESR signal [49–51]. As shown in Fig. 10a,b, no signal was observed in all three tested catalysts under dark conditions (gray curves). With illumination, the characteristic signal peaks of DMPO-·OH with relative amplitude of 1:2:2:1 were generated in $W_{18}O_{49}$ and W20-CNNT, but not in CNNT. This is because the VB potential in CNNT is too negative than that of OH^-/·OH (1.99 eV) to produce ·OH species [52]. The weak signal of $\cdot O_2^-$ radicals can be observed in the presence of the $W_{18}O_{49}$, which indicates that the high-energy "hot electrons" generated by the LSPR effect can directly drive the oxygen reduction reaction to produce $\cdot O_2^-$, since the CB position of $W_{18}O_{49}$ (0.22 V) is not negative enough to convert O_2 to $\cdot O_2^-$ (-0.33 V) [22,53]. In addition, the DMPO-$\cdot O_2^-$ and DMPO-·OH signals in W20-CNNT were stronger than those in $W_{18}O_{49}$ and CNNT after irradiation, indicating the generation of more $\cdot O_2^-$ and ·OH radicals. These radicals can serve as reactive active species for both the photocatalytic degradation and sterilization. The radical trapping experiments in Fig. S20 demonstrate that the ·OH and h^+ radicals play vital roles in photocatalytic degradation. The above results further verified that the $W_{18}O_{49}$/g-C_3N_4 heterojunction was constructed according to the S-scheme alignment (Fig. 10c). Under illumination of 420–450 nm, the e^- in g-C_3N_4 and $W_{18}O_{49}$ can be excited to their respective conduction bands, while h^+ are retained in their valence bands. A small number of "hot electrons" generated by the LSPR effect of $W_{18}O_{49}$ are injected into CB of g-C_3N_4 when irradiated at 600–700 nm wavelengths (Fig. 7l). The e^- in the CB of $W_{18}O_{49}$ recombines with h^+ in the VB of g-C_3N_4, preserving the e^- (from g-C_3N_4) and h^+ (from $W_{18}O_{49}$) with higher redox ability. The e^- can reduce H^+ to produce H_2, while a part of h^+ (from $W_{18}O_{49}$) directly participates in the photocatalytic oxidation reaction, and the other part of h^+ oxidizes OH^- to ·OH. The h^+ and ·OH with strong oxidation can not only degrade RhB into nontoxic small molecules, but also destroy the cell membrane and intracellular substances of *E. coli*, inactivate bacteria and prevent bacterial reproduction [54], thus achieving a multifunctional catalytic effect.

4. Conclusions

In summary, an S-scheme $W_{18}O_{49}$/g-C_3N_4 heterojunction photocatalyst was developed through decorating the $W_{18}O_{49}$ nanowires on the double-layer hollow g-C_3N_4 nanotubes, which could serve as a high-efficiency and multifunctional photocatalyst for photocatalytic hydrogen production, degradation and bactericidal properties, realizing the role of "one stone, three birds". The photocatalytic hydrogen evolution rate of W20-CNNT (4.67 $mmol \cdot g^{-1} \cdot h^{-1}$) was approximately 15.1 times that of Bulk-CN. When utilizing the photogenerated holes, the as-established S-scheme heterojunction photocatalyst enabled the degradation rate of RhB achieved 100 % within 12 min, and the bactericidal rate against *E. coli* reached 99.41 % within 20 min, exhibiting the ultrafast degradation and bactericidal performances. Considering the three steps of photocatalytic reaction process, including light absorption characteristics, carrier separation and transfer, and surface redox reaction of catalyst, the reasons and mechanisms for the enhancement of photocatalytic performances were systematically analyzed through FDTD simulations, DFT calculations and a series of experimental results. The analysis and exploration in this paper might pave the way for further development of efficient multifunctional photocatalysts for more sustainable applications.

CRediT authorship contribution statement

Yaru Shang: Conceptualization, Methodology, Data curation, Writing – original draft. **Chunliang Wang:** Software, Writing – review & editing. **Chunshuang Yan:** Funding acquisition, Supervision, Writing – review & editing. **Fengyang Jing:** . **Morteza Roostaeinia:** . **Yu Wang:** Funding acquisition, Writing – review & editing, Supervision. **Gang Chen:** Supervision. **Chade Lv:** Formal analysis, Writing – review & editing.

Data availability

No data was used for the research described in the article.

Declaration of Competing Interest

The authors declare that they have no known competing financial interests or personal relationships that could have appeared to influence the work reported in this paper.

Acknowledgments

This work was financially supported by projects of Natural Science Foundation of Heilongjiang Province, China (LH2021B009). C.Y. acknowledges funding supported by the National Natural Science Foundation of China (grant no. 52101246), the Fundamental Research Funds for the Central Universities and Natural Science Foundation of Heilongjiang Province, China (YQ2022B006).

Appendix A. Supplementary material

Supplementary data to this article can be found online at https://doi.org/10.1016/j.jcis.2022.12.039.

References

[1] Z. Mo, J. Di, P. Yan, C. Lv, X. Zhu, D. Liu, Y. Song, C. Liu, Q. Yu, H. Li, Y. Lei, H. Xu, Q. Yan, An all-organic D-A system for visible-light-driven overall water splitting, Small 16 (2020) 2003914, https://doi.org/10.1002/smll.202003914.
[2] H. Bai, S.H. Lam, J. Yang, X. Cheng, S. Li, R. Jiang, L. Shao, J. Wang, A schottky-barrier-free plasmonic semiconductor photocatalyst for nitrogen fixation in a "one-stone-two-birds" manner, Adv. Mater. 34 (2022) 2104226, https://doi.org/10.1002/adma.202104226.
[3] D. Zhao, Y. Wang, C.L. Dong, Y.C. Huang, J. Chen, F. Xue, S. Shen, L. Guo, Boron-doped nitrogen-deficient carbon nitride-based Z-scheme heterostructures for photocatalytic overall water splitting, Nat. Energy 6 (2021) 388–397, https://doi.org/10.1038/s41560-021-00795-9.
[4] Y. Shang, Y. Wang, C. Lv, F. Jing, T. Liu, W. Li, S. Liu, G. Chen, A broom-like tube-in-tube bundle O-doped graphitic carbon nitride nanoreactor that promotes photocatalytic hydrogen evolution, Chem. Eng. J. 431 (2022), https://doi.org/10.1016/j.cej.2021.133898 133898.
[5] L. Behera, B. Barik, S. Mohapatra, Improved photodegradation and antimicrobial activity of hydrothermally synthesized 0.2Ce-TiO_2/RGO under visible light, Colloids and Surfaces A: Physicochem. Eng. Aspects 620 620 (2021) 126553.
[6] Y.C. Nie, F. Yu, L.C. Wang, Q.J. Xing, X. Liu, Y. Pei, J.P. Zou, W.L. Dai, Y. Li, S.L. Suib, Photocatalytic degradation of organic pollutants coupled with simultaneous photocatalytic H_2 evolution over graphene quantum dots/Mn-N-TiO_2/g-C_3N_4 composite catalysts: Performance and mechanism, Appl. Catal. B Environ. 227 (2018) 312–321, https://doi.org/10.1016/j.apcatb.2018.01.033.
[7] X. Xiao, Y. Gao, L. Zhang, J. Zhang, Q. Zhang, Q. Li, H. Bao, J. Zhou, S. Miao, N. Chen, J. Wang, B. Jiang, C. Tian, H. Fu, A promoted charge separation/transfer system from Cu single atoms and C_3N_4 layers for efficient photocatalysis, Adv. Mater. 32 (2020) 2003082, https://doi.org/10.1002/adma.202003082.
[8] Y. Zou, K. Xiao, Q. Qin, J.W. Shi, T. Heil, Y. Markushyna, L. Jiang, M. Antonietti, A. Savateev, Enhanced organic photocatalysis in confined flow through a carbon nitride nanotube membrane with conversions in the millisecond regime, ACS Nano 15 (2021) 6551–6561, https://doi.org/10.1021/acsnano.0c09661.
[9] H. Xu, X. She, T. Fei, Y. Song, D. Liu, H. Li, X. Yang, J. Yang, H. Li, L. Song, P.M. Ajayan, J. Wu, Metal-oxide-mediated subtractive manufacturing of twodimensional carbon nitride for high-efficiency and high-yield photocatalytic H_2 evolution, ACS Nano 13 (2019) 11294–11302, https://doi.org/10.1021/acsnano.9b04443.

[10] Y.C. Chu, T.J. Lin, Y.R. Lin, W.L. Chiu, B.S. Nguyen, C. Hu, Influence of P, S, O-Doping on g.C_3N4 for hydrogel formation and photocatalysis: An experimental and theoretical study, Carbon 169 (2020) 338–348, https://doi.org/10.1016/j.carbon.2020.07.053.
[11] G. Wang, T. Zhang, W. Yu, R. Si, Y. Liu, Z. Zhao, Modulating location of single copper atoms in polymeric carbon nitride for enhanced photoredox catalysis, ACS Catal. 10 (2020) 5715–5722, https://doi.org/10.1021/acscatal.0c01099.
[12] G. Li, X. Deng, P. Chen, X. Wang, J. Ma, F. Liu, S.F. Yin, Sulphur vacancies-VS_2@C_3N_4 drived by in situ supramolecular self-assembly for synergistic photocatalytic degradation of real wastewater and H_2 production: Vacancies taming interfacial compact heterojunction and carriers transfer, Chem. Eng. J. 433 (2022), https://doi.org/10.1016/j.cej.2022.134505 134505.
[13] M.F.R. Samsudin, C. Frebillot, Y. Kaddoury, S. Sufian, W.J. Ong, Bifunctional Z-scheme Ag/$AgVO_3$/g-C_3N_4 photocatalysts for expired ciprofloxacin degradation and hydrogen production from natural rainwater without using scavengers, J. Environ. Manage. 270 (2020), https://doi.org/10.1016/j.jenvman.2020.110803 110803.
[14] B. Li, B. Zhang, Y. Zhang, M. Zhang, W. Huang, C. Yu, J. Sun, J. Feng, S. Dong, J. Sun, Porous g-C_3N_4/TiO_2 S-scheme heterojunction photocatalyst for visible-light driven H_2 production and simultaneous wastewater purification, Int. J. Hydrogen Energy 46 (2021) 32413–32424, https://doi.org/10.1016/j.ijhydene.2021.07.090.
[15] C. Lv, Y. Qian, C. Yan, Y. Ding, Y. Liu, G. Chen, G. Yu, Defect engineering metal-free polymeric carbon nitride electrocatalyst for effective nitrogen fixation under ambient conditions, Angew. Chem. Int. Ed. 57 (2018) 10246–10250, https://doi.org/10.1002/anie.201806386.
[16] Z. Jiang, C. Jia, B.o. Wang, P. Yang, G. Gao, Hexagonal g-C_3N_4 nanotubes with Pt decorated surface towards enhanced photo- and electro-chemistry performance, J. Alloys Compd. 826 (2020) 154145, doi:10.1016/j.jallcom.2020.154145.
[17] Y. Ren, D. Feng, Z. Yan, Z. Sun, Z. Zhang, D. Xu, C. Qiao, Z. Chen, Y.u. Jia, S. Chan Jun, S. Liu, Y. Yamauchi, Interfacial coupled engineering of plasmonic amorphous MoO_{3-x} nanodots/g-C_3N_4 nanosheets for photocatalytic water splitting and photothermal conversion, Chem. Eng. J. 453 (2023) 139875, https://doi.org/10.1016/j.cej.2022.139875.
[18] C. Feng, L. Tang, Y. Deng, J. Wang, W. Tang, Y. Liu, Z. Chen, J. Yu, J. Wang, Q. Liang, Synthesis of branched WO_3@$W_{18}O_{49}$ homojunction with enhanced interfacial charge separation and full-spectrum photocatalytic performance, Chem. Eng. J. 389 (2020), https://doi.org/10.1016/j.cej.2020.124474 124474.
[19] J. Cui, Y. Li, L. Liu, L. Chen, J. Xu, J. Ma, G. Fang, E. Zhu, H. Wu, L. Zhao, L. Wang, Y. Huang, Near-infrared plasmonic-enhanced solar energy harvest for highly efficient photocatalytic reactions, Nano Lett. 15 (2015) 6295–6301, https://doi.org/10.1021/acs.nanolett.5b00950.
[20] T. Song, X. Zhang, P. Yang, Bifunctional nitrogen-doped carbon dots in g-C_3N_4/WO_x heterojunction for enhanced photocatalytic water-splitting performance, Langmuir 37 (2021) 4236–4247, https://doi.org/10.1021/acs.langmuir.1c00210.
[21] C. Feng, L. Tang, Y. Deng, J. Wang, Y. Liu, X. Ouyang, Z. Chen, H. Yang, J. Yu, J. Wang, Maintaining stable LSPR performance of $W_{18}O_{49}$ by protecting its oxygen vacancy: A novel strategy for achieving durable sunlight driven photocatalysis, Appl. Catal. B Environ. 276 (2020), https://doi.org/10.1016/j.apcatb.2020.119167 119167.
[22] M. Wang, G. Tan, M. Dang, Y. Wang, B. Zhang, H. Ren, L. Lv, A. Xia, Dual defects and build-in electric field mediated direct Z-scheme $W_{18}O_{49}$/g-C_3N_{4-x} heterojunction for photocatalytic NO removal and organic pollutant degradation, J. Colloid Interface Sci. 582 (2021) 212–226, https://doi.org/10.1016/j.jcis.2020.08.040.
[23] Y. Shang, Y. Cui, R. Shi, A. Zhang, Y. Wang, P. Yang, Self-reduction combined with photo-deposition decorating Au nanoparticles on urchin-like $WO_{2.72}$ for enhancement of trimethylamine-sensing performance, Mater. Sci. Semicond. Process. 101 (2019) 131–138, https://doi.org/10.1016/j.mssp.2019.05.037.
[24] Z. Zhang, J. Huang, Y. Fang, M. Zhang, K. Liu, B. Dong, A nonmetal plasmonic Z-scheme photocatalyst with UV- to NIR-driven photocatalytic protons reduction, Adv. Mater. 29 (2017) 1606688, https://doi.org/10.1002/adma.201606688.
[25] Y. Shang, R. Shi, Y. Cui, Q. Che, J. Wang, P. Yang, Urchin-like $WO_{2.72}$ microspheres decorated with Au and PdO nanoparticles for the selective detection of trimethylamine, ACS Appl, Nano Mater. 3 (2020) 5554–5564, https://doi.org/10.1021/acsanm.0c00827.
[26] C. Lv, L. Zhong, Y. Yao, D. Liu, Y.i. Kong, X. Jin, Z. Fang, W. Xu, C. Yan, K.N. Dinh, M. Shao, L.i. Song, G. Chen, S. Li, Q. Yan, G. Yu, Boosting electrocatalytic ammonia production through mimicking "π back-donation", Chem 6 (10) (2020) 2690–2702, https://doi.org/10.1016/j.chempr.2020.07.006.
[27] Y. Jiang, Z. Sun, C. Tang, Y. Zhou, L. Zeng, L. Huang, Enhancement of photocatalytic hydrogen evolution activity of porous oxygen doped g-C_3N_4 with nitrogen defects induced by changing electron transition, Appl. Catal. B Environ. 240 (2019) 30–38, https://doi.org/10.1016/j.apcatb.2018.08.059.
[28] Y. Shang, X. Cheng, R. Shi, Q. Ma, Y. Wang, P. Yang, Synthesis and comparative investigation of adsorption capability and photocatalytic activities of WO_3 and $W_{18}O_{49}$, Mater. Sci. Eng., B 262 (2020) 114724, https://doi.org/10.1016/j.mseb.2020.114724.
[29] Z. Jiang, X. Zhang, H.S. Chen, P. Yang, S.P. Jiang, Fusiform-shaped g-C_3N_4 capsules with superior photocatalytic activity, Small 16 (2020) 2003910, https://doi.org/10.1002/smll.202003910.
[30] C. Lv, L. Zhong, H. Liu, Z. Fang, C. Yan, M. Chen, Y. Kong, C. Lee, D. Liu, S. Li, J. Liu, L. Song, G. Chen, Q. Yan, G. Yu, Selective electrocatalytic synthesis of urea with nitrate and carbon dioxide, Nat. Sustain. 4 (2021) 868–876, https://doi.org/10.1038/s41893-021-00741-3.
[31] J. Fu, Q. Xu, J. Low, C. Jiang, J. Yu, Ultrathin 2D/2D WO_3/g-C_3N_4 step-scheme H_2 production photocatalyst, Appl. Catal. B Environ. 243 (2019) 556–565, https://doi.org/10.1016/j.apcatb.2018.11.011.
[32] X. Jin, C. Lv, X. Zhou, H. Xie, S. Sun, Y. Liu, Q. Meng, G. Chen, A bismuth rich hollow $Bi_4O_5Br_2$ photocatalyst enables dramatic CO_2 reduction activity, Nano Energy 64 (2019), https://doi.org/10.1016/j.nanoen.2019.103955 103955.
[33] Y.H. Jang, Y.J. Jang, S. Kim, L.N. Quan, K. Chung, D.H. Kim, Plasmonic solar cells: From rational design to mechanism overview, Chem. Rev. 116 (2016) 14982–15034, https://doi.org/10.1021/acs.chemrev.6b00302.
[34] Y. Li, Z. Ruan, Y. He, J. Li, K. Li, Y. Yang, D. Xia, K. Lin, Y. Yuan, Enhanced photocatalytic H_2 evolution and phenol degradation over sulfur doped meso/macroporous g-C_3N_4 spheres with continuous channels, Int. J. Hydrogen Energy 44 (2019) 707–719, https://doi.org/10.1016/j.ijhydene.2018.10.124.
[35] Y. Shi, Q. Liu, R. Hong, C. Tao, Q. Wang, H. Lin, Z. Han, D. Zhang, SERS-active WO_{3-x} thin films with tunable surface plasmon resonance induced by defects from thermal treatment, Spectrochim. Acta, Part A 268 (2022), https://doi.org/10.1016/j.saa.2021.120686 120686.
[36] W. Wu, X. Li, Z. Ruan, Y. Li, X. Xu, Y. Yuan, K. Lin, Fabrication of a TiO_2 trapped meso/macroporous g-C_3N_4 heterojunction photocatalyst and understanding its enhanced photocatalytic activity based on optical simulation analysis, Inorg Chem Front 5 (2018) 481–489, https://doi.org/10.1039/C7QI00751E.
[37] Y. Liang, X. Wu, X. Liu, C. Li, S. Liu, Recovering solar fuels from photocatalytic CO_2 reduction over W^{6+}-incorporated crystalline g-C_3N_4 nanorods by synergetic modulation of active centers, Appl. Catal. B Environ. 304 (2022), https://doi.org/10.1016/j.apcatb.2021.120978 120978.
[38] C. Lv, C. Lee, L. Zhong, H. Liu, J. Liu, L. Yang, C. Yan, W. Yu, H.H. Hng, Z. Qi, L.i. Song, S. Li, K.P. Loh, Q. Yan, G. Yu, A defect engineered electrocatalyst that promotes high-efficiency urea synthesis under ambient conditions, ACS Nano 16 (5) (2022) 8213–8222, doi:10.1021/acsnano.2c01956.
[39] F. He, G. Chen, J. Miao, Z. Wang, D. Su, S. Liu, W. Cai, L. Zhang, S. Hao, B. Liu, Sulfur-mediated self-templating synthesis of tapered C-PAN/g-C_3N_4 composite nanotubes toward efficient photocatalytic H_2 evolution, ACS Energy Lett. 1 (2016) 969–975, https://doi.org/10.1021/acsenergylett.6b00398.
[40] J. Liu, Y. Yu, R. Qi, C. Cao, X. Liu, Y. Zheng, W. Song, Enhanced electron separation on in-plane benzene-ring doped g-C_3N_4 nanosheets for visible light photocatalytic hydrogen evolution, Appl. Catal. B Environ. 244 (2019) 459–464, https://doi.org/10.1016/j.apcatb.2018.11.070.
[41] Y. Dai, Y.J. Xiong, Control of selectivity in organic synthesis via heterogeneous photocatalysis under visible light, Nano Res. Energy . 1 (2022), https://doi.org/10.26599/NRE.2022.9120006 e9120006.
[42] G. Li, Z. Xie, S. Chai, X. Chen, X. Wang, A facile one-step fabrication of holey carbon nitride nanosheets for visible-light-driven hydrogen evolution, Appl. Catal. B Environ. 283 (2021), https://doi.org/10.1016/j.apcatb.2020.119637 119637.
[43] N. Lu, Z. Zhang, Y. Wang, B. Liu, L. Guo, L. Wang, J. Huang, K. Liu, B. Dong, Direct evidence of IR-driven hot electron transfer in metal-free plasmonic $W_{18}O_{49}$/Carbon heterostructures for enhanced catalytic H_2 production, Appl. Catal. B Environ. 233 (2018) 19–25, https://doi.org/10.1016/j.apcatb.2018.03.073.
[44] Z. Zhang, X. Jiang, B. Liu, L. Guo, N. Lu, L. Wang, J. Huang, K. Liu, B. Dong, IR-driven ultrafast transfer of plasmonic hot electrons in nonmetallic branched heterostructures for enhanced H_2 generation, Adv. Mater. 30 (2018) 1705221, https://doi.org/10.1002/adma.201705221.
[45] Y. Yang, Y. Cong, X. Lin, B. Cao, D. Dong, K. Liu, Y. Xiao, J. Shang, Y. Bao, Y. Liu, G. Fang, Y. Wang, Y. Chen, J. Zhang, B. Dong, Dual LSPR of Au/$W_{18}O_{49}$ heterostructures for upconversion enhancement and application of molecular detection, J. Mater. Chem. A 8 (2020) 4040–4048, https://doi.org/10.1039/C9TA13466B.
[46] Q. Liu, X. He, J. Peng, X. Yu, H. Tang, J. Zhang, Hot-electron-assisted S-scheme heterojunction of tungsten oxide/graphitic carbon nitride for broad-spectrum photocatalytic H_2 generation, Chin. J. Catal. 42 (2021) 1478–1487, https://doi.org/10.1016/S1872-2067(20)63753-6.
[47] A. Sabbah, I. Shown, M. Qorbani, F.Y. Fu, T.Y. Lin, H.L. Wu, P.W. Chung, C.I. Wu, S.R.M. Santiago, J.L. Shen, K.H. Chen, L.C. Chen, Boosting photocatalytic CO_2 reduction in a ZnS/$ZnIn_2S_4$ heterostructure through strain-induced direct Z-scheme and a mechanistic study of molecular CO_2 interaction thereon, Nano Energy 93 (2022), https://doi.org/10.1016/j.nanoen.2021.106809 106809.
[48] C.H. Shen, X.J. Wen, Z.H. Fei, Z.T. Liu, Q.M. Mu, Novel Z-scheme $W_{18}O_{49}$/CeO_2 heterojunction for improved photocatalytic hydrogen evolution, J. Colloid Interface Sci. 579 (2020) 297–306, https://doi.org/10.1016/j.jcis.2020.06.075.
[49] H. Gao, H. Yang, J. Xu, S. Zhang, J. Li, Strongly coupled g-C_3N_4 nanosheets-Co_3O_4 quantum dots as 2D/0D heterostructure composite for peroxymonosulfate activation, Small 14 (2018) 1801353, https://doi.org/10.1002/smll.201801353.
[50] Y. Shi, Q. Zhao, J. Li, G. Gao, J. Zhi, Onion-liked carbon-embedded graphitic carbon nitride for enhanced photocatalytic hydrogen evolution and dye degradation, Appl. Catal. B Environ. 308 (2022), https://doi.org/10.1016/j.apcatb.2022.121216 121216.
[51] F.A. Qaraah, S.A. Mahyoub, A. Hezam, A. Qaraah, F. Xin, G. Xiu, Synergistic effect of hierarchical structure and S-scheme heterojunction over O-doped g-C_3N_4/N-doped Nb_2O_5 for highly efficient photocatalytic CO_2 reduction, Appl. Catal. B Environ. 315 (2022), https://doi.org/10.1016/j.apcatb.2022.121585 121585.

[52] Y. Jiang, H.Y. Chen, J.Y. Li, J.F. Liao, H.H. Zhang, X.D. Wang, D.B. Kuang, Z-scheme 2D/2D heterojunction of CsPbBr 3/B_i2W_O6 for improved photocatalytic C_O2 reduction, Adv. Funct. Mater. 30 (2020) 2004293, https://doi.org/10.1002/adfm.202004293.
[53] Y. Lu, X. Jia, Z. Ma, Y. Li, S. Yue, X. Liu, J. Zhang, W^{5+}-W^{5+} pair induced LSPR of $W_{18}O_{49}$ to sensitize $ZnIn_2S_4$ for full-spectrum solar-light-driven photocatalytic hydrogen evolution, Adv. Funct. Mater. 32 (2022) 2203638, https://doi.org/10.1002/adfm.202203638.
[54] P. Li, J. Li, X. Feng, J. Li, Y. Hao, J. Zhang, H. Wang, A. Yin, J. Zhou, X. Ma, B. Wang, Metal-organic frameworks with photocatalytic bactericidal activity for integrated air cleaning, Nat. Commun. 10 (2019) 2177, https://doi.org/10.1038/s41467-019-10218-9.